A biomimetic and bioactive scaffold with intelligently pulsatile teriparatide delivery for local and systemic osteoporosis regeneration

Lingbin Che [a],[1], Ying Wang [b],[1], Dongyong Sha [b], Guangyi Li [c], Ziheng Wei [a], Changsheng Liu [b], Yuan Yuan [b],[*], Dianwen Song [a],[**]

[a] Department of Orthopedics, Shanghai General Hospital, Shanghai Jiaotong University School of Medicine, Shanghai, 200080, PR China
[b] Key Laboratory for Ultrafine Materials of Ministry of Education, Frontiers Science Center for Materiobiology and Dynamic Chemistry and School of Materials Science and Engineering, East China University of Science and Technology, Shanghai 200237, PR China
[c] Shanghai Advanced Research Institute, Chinese Academy of Sciences, Shanghai, 201210, PR China

ARTICLE INFO

ABSTRACT

Osteoporosis is one of the most disabling consequences of aging, osteoporotic fractures and higher risk of the subsequent fractures leading to substantial disability and deaths, indicating both local fractures healing and the early anti-osteoporosis therapy are of great significance. Teriparatide is strong bone formation promoter effective in treating osteoporosis, while side effects limit clinical applications. Traditional drug delivery is lack of sensitive and short-term release, finding a new non-invasive and easily controllable drug delivery to not only repair the local fractures but also improve total bone mass has remained a great challenge. Thus, bioinspired by the natural bone components, we develop appropriate interactions between inorganic biological scaffolds and organic drug molecules, achieving both loaded with the teriparatide in the scaffold and capable of releasing on demand. Herein, biomimetic bone microstructure of mesoporous bioglass, a near-infrared ray triggered switch, thermo-sensitive liposomes based on a valve, and polydopamine coated as a heater is developed rationally for osteoporotic bone regeneration. Teriparatide is pulsatile released from intelligent delivery, not only rejuvenating osteoporotic bone defect, but also presenting strong systemic anti-osteoporosis therapy. This biomimetic bone carrying novel drug delivery platform is well worth expecting to be a new promising strategy and clinically commercialized to help patients survive from the osteoporotic fracture.

1. Introduction

Osteoporosis, a bone disease characterized by bone loss and micro-architectural deterioration, is one of the most disabling consequences of aging [1], and approximately 9 million osteoporotic fractures occur worldwide each year [2–4]. In China, the number of osteoporotic fractures in 2010 was approximately 2.3 million, with an estimated subsequent increase to 6 million by 2050 [5]. Compared with normal bone fractures, the repair of osteoporotic fractures is particularly challenging due to their compromised skeletal strength, lower density, trabecular microstructure and bone-forming ability [6], and a higher requirement is put forward for the activity of biomaterials. Furthermore, 23% and 54.3% of the subsequent fractures occurred within one and five years,

respectively [7], indicating more attention needs to be paid to systemic osteoporosis treatment.

Teriparatide is the few approved prescription of a bone formation promoter worldwide [3,8], with the amazing efficacy to reduce the risk of vertebral fractures by 65% [8,9]. Currently, intermittent daily subcutaneous injection is recommended in clinical in despite of pain and needles fear, with insufficient local bioavailability in the osteoporotic bone fracture area [10]. Once increasing the dosage, the consequent systemic side effects such as strong bone resorption and hypercalcemia [11] may cause arrhythmias and even potential life threats. How to achieve the precise pulse release of the teriparatide according to the concentration of blood calcium is still of great difficulty.

Bone tissue engineering scaffolds hold great promise for the

treatment of osteoporotic bone defects. However, most of bone tissue engineering scaffolds focus only on the local osteoporotic bone regeneration [12,13], and traditional drug delivery systems are based on distinct erosion or degradation speed between components to achieve the controllable release [14–19], with their limited application by inactive intervention *in vivo*. Recently, thermo sensitive liposomes (TSLs) are easily controlled by temperature to achieve stable retention or rapid drug release [20,21]. The extravasation of TSLs would be enhanced significantly when system temperature rises above the transition temperature, causing an immediate and rapid release of payloads [22]. While once the temperature is below the transition temperature, liposomes quickly recover to dense structure and are stable with seldom drug release. Nowadays, stimuli-responsive devices are developed to fabricate smart devices, especially Near InfraRed (NIR), considering its deep penetration through tissues and acute control of temperature [23, 24]. Xia et al. [25–28] developed microparticles made of thermo-sensitive phase-change material (PCM) encapsulating photosensitive NIR dye, to achieve pulse drug release. As for NIR triggered system, the heater of high photothermal conversion efficiency and the valve of thermo sensitivity are determinant. Polydopamine (PDA) is a photo-responsive material that has an excellent light absorption ability due to its high molar extinction coefficient [29], and also a strong adhesive bioinspired by the mussel [30]. It represents high photothermal conversion efficiency up to 40% under NIR due to its high molar extinction coefficient [29], and would be coated onto various surfaces via in-situ polymerization of dopamine [31]. Mesoporous bioglass (MBG), rich in calcium and phosphorus, mimicking the hierarchical microporous structure of natural bone, has been considered an effective strategy to facilitate early implant integration with the host bone [32] and a well drug storage system. Therefore, it is conceived that the incorporation of thermo sensitive liposomes into PDA coated MBG would endow precise pulse release of teriparatide with NIR responsive features for bionic bone tissue engineering applications. On the other hand, it is well-accepted that the essential processes for a classical bone regeneration mainly include cell recruitment, proliferation, osteogenic differentiation, and biomineralization, while the early stage, particularly in the first 14 days, playing the most critical role in the whole bone regeneration [33,34]. Accelerating migration of stem cells [35], promoting blood vessel migration [33], and increasing the inflammatory response [36] and immune modulating [37] at the early stage all promoted the bone regeneration. Therefore, the ideal delivery system designed should release PTH for the early 14 days.

Herein, bioinspired by natural bone structure, we develop the biomimetic bone structure that fully considers the need for appropriate interactions between inorganic biological scaffolds and organic powerful osteogenic teriparatide, achieving both firmly loaded with teriparatide in the scaffold and capable of releasing on demand. Bridged by the sensitive photothermal response and strong adhesive coating, we realized the local precise pulse teriparatide release to both rejuvenate osteoporotic bone defect and systemically treat osteoporosis. Meanwhile, all components are well suited for clinical translation. In a word, this intelligent device is a novel promising therapy for osteoporotic fracture patients and is well worth expecting in clinical commercialization.

2. Materials and methods

2.1. Materials

Tetraethylorthosilicate (TEOS, analytical grade) and concentrated hydrochloric acid (HCl, 37.5%, analytical grade) were purchased from Shanghai Lingfeng Chemical Reagent Co., Ltd. Absolute ethanol (analytical grade), triethyl phosphate (analytical grade), and calcium nitrate tetrahydrate (Ca(NO$_3$)$_2$•4H$_2$O, analytically pure) were purchased from Sinopharm Chemical Reagent Company. 1,2-dihexadecanoyl-rac-*glycero*-3-phosphocholine (DPPC), diethyl phosphor-ocyanidate (DEPC), cholesterol, and Distearoyl phosphoethanolamine-PEG2000 (DSPE-PEG2000) were purchased from Sigma Aldrich Company (Shanxi, China), and teriparatide was purchased from Peptides Biotech Co. (Zhejiang, China). Calcein, F127 (EO$_{106}$PO$_{70}$EO$_{106}$), fluorescein isothiocyanate (FITC)-phalloidin, and *para*-nitrophenyl phosphate were purchased from Sigma-Aldrich (USA). Fetal bovine serum (FBS) and minimum essential medium were purchased from Gibco® (Thermo Fisher Scientific Inc., MA, USA).

2.2. Fabrication of liposome-loaded teriparatide

Thermosensitive liposomes were prepared using a membrane dispersion method [38]. Briefly, DPPC or DEPC, cholesterol, and DSPE-PEG2000 at a molar ratio of 60:35:5 were dissolved in chloroform with calcein blended in ethanol. The solvent was removed under nitrogen gas, followed by vacuum drying for 2 h. Afterward, the dried lipid films were hydrated at 45 °C with phosphate buffer saline (PBS) or 2 mg mL^{-1} teriparatide solution for 1 h and then extruded through a polycarbonate membrane of 100 nm. The morphology was viewed by cryo-transmission electron microscopy (Cy-TEM, Tecnai G2 F20 200 kV). The phase-transition temperature was measured by differential scanning calorimetry (DSC, DIAMOND8500), and the fluorescence intensity of released calcein was measured under Triton-X at 37 °C and 42 °C.

2.3. Fabrication of controlled release platforms

MBG scaffolds with a three-dimensional pore structure were synthesized by a rapid sol-gel method. Then, the MBG scaffolds were immersed in a stirring dopamine/Tris-HCl solution (pH = 8.5) at room temperature for 1 h, causing in situ polymerization on the interface to fabricate a PDA-coated MBG scaffold (MBG-PDA). Then, liposomes were loaded on the PDA coating scaffold via physical adsorption. DPPC liposomes were loaded on MBG-PDA scaffolds, while DEPC liposomes were loaded onto MBG scaffolds. The morphology of the scaffolds loaded with liposomes was further analyzed using scanning electron microscope (SEM) (Hitachi S-4800).

2.4. NIR-triggered release in vitro and in vivo

Under laser irradiation at different power densities (0.5 W cm^{-2} and 0.9 W cm^{-2}), the rise in temperature of the wet scaffolds was recorded using an infrared camera (FOTRIC 220S, FOTRIC INC, Shanghai). Calcein was chosen as a payload for *in vitro* and *in vivo* triggered release observations. Liposomes encapsulating calcein were loaded onto the PDA-MBG scaffold. For *in vitro* release, a calcein-loaded PDA-MBG scaffold was tested before and after irradiation utilizing laser confocal scanning microscopy (CLSM A1, Nikon, Japan). For *in vivo* release upon irradiation, calcein-loaded PDA-MBG cylinders of Φ4 mm × 1.5 mm were implanted into calvarial bone, and the fluorescence intensity was evaluated every day for 7 days by *in vivo* fluorescence imaging (ViewnVivo B30, Optiscan, Australia). The amount of released teriparatide was assessed by a human teriparatide enzyme linked immunosorbent assay (ELISA) kit (Quidel, America). The bioactivities of the native and released teriparatide were evaluated and compared using circular dichroism (J-1500, Jasco, Japan). Compression tests were measured on a universal mechanical test system (CMT4104).

2.5. In vitro biocompatibility and bioacitve evaluation

Bone marrow stromal cells (BMSCs) were obtained from Sprague-Dawley rats and were routinely cultured in α-minimum essential medium supplemented with 10% FBS and 1% antibiotics. BMSCs were seeded onto MBG and MBG-PDA scaffolds at a density of 2 × 10^4 cells per Φ4 mm × 1.5 mm scaffolds. BMSCs were first fixed with 2.5% (v/v) glutaraldehyde at 4 °C for 15 min and then incubated with FITC-

phalloidin (5 μg mL^{-1}) at 37 °C for 45 min. The cell distribution was imaged by 3D CLSM from bottom to top. An Alamar Blue assay kit was utilized to study the cytotoxicity of the scaffolds. Briefly, BMSCs were seeded onto scaffolds at a density of 5×10^3 cells per scaffold for 1, 4, and 7 days. At each time point, scaffolds were gently rinsed with 200 μL of a mixture solution of fresh medium and Alamar Blue solution (v/v = 9:1) for 2 h. Then, 100 μL of the mixture was measured by a spectrophotometric microplate reader (Multiskan Sky High, Thermo Fisher; ex: 520 nm/em: 590 nm). Similarly, to evaluate cell viability under NIR irradiation, M/P-NIR (NIR-irradiated MBG-PDA) and Pulsatile group scaffolds seeded with BMSCs were exposed to NIR light every day at a power density of 0.5 W cm^{-2} for 40 s.

An alkaline phosphatase (ALP) detection kit was utilized to evaluate the bioactivity of released teriparatide further and whether the pulsatile release of teriparatide can improve osteogenic differentiation. Briefly, BMSCs were seeded onto scaffolds at a density of 2×10^4 cells per scaffold for 7 and 14 days. For M/P-NIR and Pulsatile groups, scaffolds were subjected to NIR light at a power density of 0.5 W cm^{-2} for 40 s every day. Medium containing 10 nM teriparatide was added to cells seeded on the MBG scaffolds for 4 h every day to mimic the pulsatile release of teriparatide, a group named Injection. For the ALP activity test, 100 μL of *para*-nitrophenyl phosphate solution (2.5 mg mL^{-1}) was coincubated with 50 μL of lysate until coloration. A BCIP/NBT Alkaline Phosphatase Color Development Kit (Beyotime, Shanghai) was also used to test the osteogenesis ability.

Alizarin red staining (ARS) was also employed. After 21 days culturing at a seeding density of 1×10^4 cells per sample, cells were fixed with 2.5% glutaraldehyde. Then, the fixed cells were rinsed with PBS twice and stained with 1% Alizarin red (pH = 4.2) for 30 min. Then, the cells on all scaffolds were rinsed with PBS and images were taken. Immunostaining of osteocalcin (OCN) was performing after 21 days of culture at a density of 1×10^4 cells per scaffold. After being fixed with 2.5% glutaraldehyde for 15 min, the cells were permeabilized with 0.1% Triton X-100 solution and blocked with 5% bovine serum albumin (BSA) for 1 h. Then, OCN was stained with mouse-*anti*-osteocalcin IgG (Abcam, HK, ab13418) at 4 °C overnight, followed by incubation with Alexa Fluor® 647 labeled goat-*anti*-mouse IgG (Abcam, HK, ab150115) for 2 h. A confocal laser scanning microscopy (CLSM, A1, Nikon, Japan) was used to examine OCN distribution of all payloads.

2.6. In vivo cranial defect model and scaffold implantation

A rat cranial defect model was applied to investigate the efficacy of scaffold osteogenic capacity in osteoporotic bone regeneration. The Animal Care and Use Committee of the School of Medicine of Shanghai Jiao Tong University approved all experimental animal procedures and animal care. After two weeks of acclimation, approximately 6-month-old female Sprague-Dawley rats underwent bilateral ovariectomy (OVX). After a 6-week development of osteoporosis, OVX rats were used to establish a critical-size calvarial defect model. In brief, after being anesthetized, the head was attached to a skull stabilizing device. Hair was shaved from the head, and the skin was sterilized with alcohol. Then, the skin and cranial periosteum were separated to expose the cranial bone. A 4 mm diameter cranial defect was made on the skull via a microbone drill. Immediately after the bone was removed, the cranial defect was rinsed with saline solution, and scaffolds were implanted. The incision was closed with several sutures. Seventy-two rats were randomly divided into six groups: (1) Sham (without treatment for cranial defects), (2) MBG, (3) NIR-irradiated MBG-PDA (M/P-NIR), (4) Injection (without teriparatide delivery devices and instead subcutaneous injection of teriparatide (40 μg/kg/d) for 14 days), (5) Continuous and (6) Pulsatile. The scaffolds of M/P-NIR and Pulsatile groups were exposed to NIR light every day at a power density of 0.5 W cm^{-2} for 30 s. After 4 and 8 weeks of implantation, rats were sacrificed, and their skulls, femurs and lumbar vertebra were harvested for Microcomputed tomography (micro-CT) analysis and histological assays.

2.7. Microcomputed tomography analysis

Micro-CT (Bruker Optik GmbH, Belgium) was used to verify the osteoporotic condition of the bones and evaluate *in vivo* bone regeneration of the platform. Skull, femur and lumbar vertebra were harvested and fixed in 4% paraformaldehyde 36 h before CT scanning. Samples were scanned at 18 μm pixel resolution (1 mm aluminum filter, 65 kV, 380 μA). The femur in Sham and OVX rats was visualized according to the coronal and transaxial planes by SkyScan CTVox and CTVol software. The analysis of the femur morphological parameter was evaluated by CTAn software, with factors such as percent bone volume (BV/TV), bone volume (BV), bone surface (BS), Bone surface density (BSD), structure model index (SMI), trabecular thickness (Tb.Th), trabecular number (Tb.N), trabecular separation (Tb.Sp) and connectivity density. The cranial defect region was visualized according to the coronal, sagittal, and transaxial planes with adjacent tissue using Dataviewer software. A cylinder-shaped region of interest (ROI) of 4-mm diameter corresponding to the defect site was selected. The analysis of the regenerated neotissue was evaluated by CTAn software, with factors such as BV, BV/TV, BS, Tb.Th, Tb.N and Tb.Sp. Representative 2D and 3D reconstruction images were acquired and processed by SkyScan Dataviewer and CTVol software, respectively. For the femur, coronal and sagittal planes were visualized, and the region 1.5 mm immediately below the growth plate was analyzed to quantify the trabecular bone volume, such as the structure model index (SMI) and BV/TV. ROIs of the 1 mm medial position of the femur and the third lumbar vertebra were reconstructed and processed by SkyScan CTVol and CTVox software, respectively.

2.8. Histological and immunohistochemical evaluation

For evaluation of bone histology, samples were fixed in 4% paraformaldehyde for 48 h and then decalcified in 10% ethylenediaminetetraacetic acid for 3 weeks before being dehydrated with gradient alcohols and embedded in paraffin, and 5 μm thick contiguous sections were sliced for hematoxylin & eosin (H&E), masson's trichrome (MT), immunohistochemistry (IHC) and Tartrate-resistant acid phosphatase (TRAP) staining analysis. For IHC staining, slides were processed by heat-induced epitope retrieval using microwave oven heating in 0.01 M citrate buffer for 9 min. The sections were incubated in diluted normal serum for an hour and then incubated with primary antibodies, including antibodies against osteopontin (OPN) (dilution 1:120, Abcam) and Runt-related transcription factor 2 (Runx2) (dilution 1:120, Abcam), at 4 °C for 24 h. After that, the sections were rinsed with PBS three times and incubated with a biotinylated secondary antibody (dilution 1:150) for 1 h. Immunoreactivity was visualized by a solution of 0.01% H$_2$O$_2$ and 0.05% diaminobenzidine that generated a brown color. Nuclei were presented with hematoxylin staining. All slides were observed by optical microscopy (Leica, Germany).

2.9. Statistical analysis

All data are presented as the mean ± standard deviation. Statistical analysis was assessed using GraphPad Prism 5.0 statistical software. All quantifications were analyzed by ImageJ software. A two-way analysis of variance was used to conduct the statistical analysis, and $p < 0.05$ was considered statistically significant.

3. Results and discussion

In this work, we developed a biomimetic bone structure for precise local pulsatile release of teriparatide to repair local osteoporotic bone defects and systemically treat osteoporosis. As shown in Fig. 1, the photothermal responsive system is based on a TSL/PDA/MBG scaffold with an interconnected pore structure. PDA is coated throughout the MBG scaffold and functions as both an adhesive to load TSLs and a
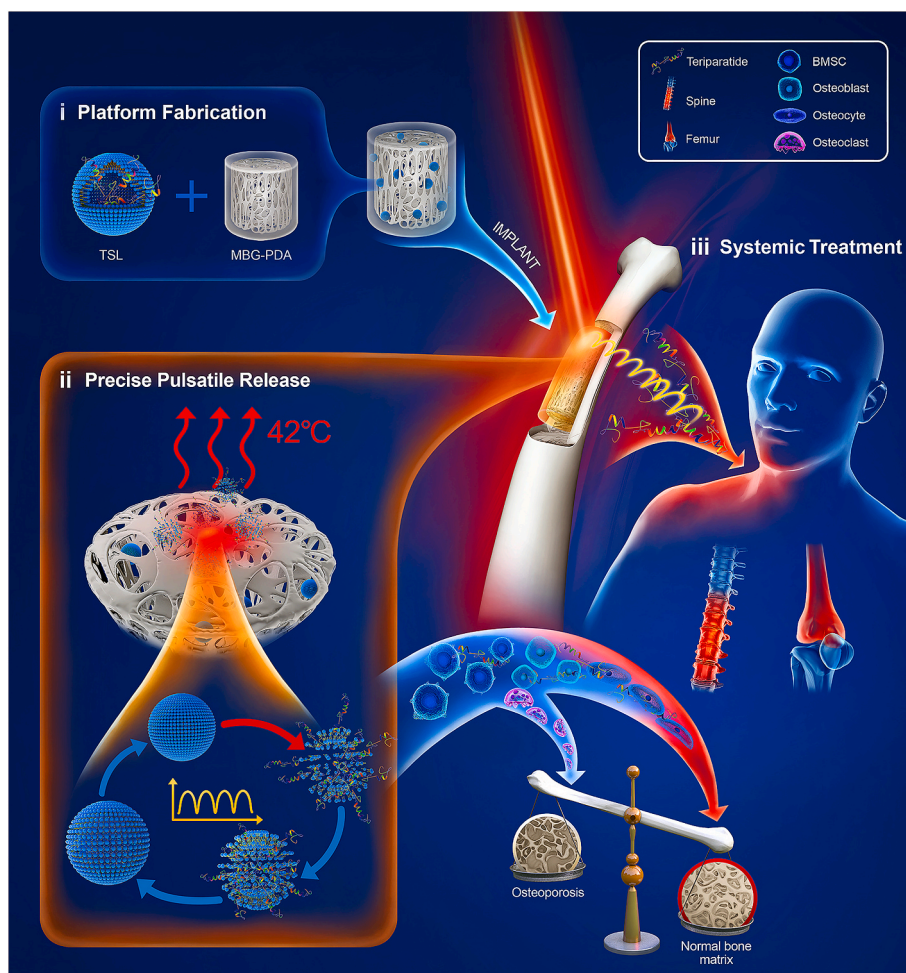
Fig. 1. Schematic illustration of the preparation process of the teriparatide delivery devices and the treatment of local bone defects and systemic osteoporosis.

heater when exposed to NIR irradiation. The TSLs next undergo a phase transition with instant release and then cool immediately without NIR light, endowing the system with spatiotemporally active pulsatile release of teriparatide, which significantly promotes osteogenic differentiation for the treatment of both local defects and systemic osteoporosis.

3.1. Characterization of TSLs and scaffold

To realize pulsatile release of teriparatide, DPPC TSLs with a transition temperature (Tm) value above physiological temperature were loaded onto PDA-MBG (Pulsatile group). For comparison, a continuous group was also fabricated utilizing DEPC TSLs having a Tm value below physiological temperature to constantly release teriparatide *in vivo*. The morphology of liposomes in Fig. 2a and b shows that both kinds of TSLs have a complete bilayer membrane structure, and the particle size of both TSLs ranges from 40 to 100 nm, with an average diameter of 70 nm. As shown in the DSC spectra in Fig. 2a and b, the T_m of the DPPC TSL was above body temperature at 41.6 °C, while the T_m of the DEPC TSL was lower at 17.0 °C. The controllable payload release from DPPC TSLs was evaluated by dispersing the nanoparticles in PBS which temperature was held below (37 °C) or above (42 °C) the Tm. Triton X solution was also utilized as a release medium for disintegration of liposome as control. As a proof-of-concept, calcein was chosen to test the thermosensitive response behavior of DPPC liposomes, as shown in Fig. 2c. The encapsulated calcein was only released when the system temperature was at 42 °C or when the liposomes were disintegrated in the Triton X solution. When the DPPC TSL was dispersed at 37 °C or room temperature, little

calcein was released. These results demonstrated that the controllable release from high-transition temperature DPPC TSLs was well realized.

The hierarchical macro/microporous structure of the MBG scaffold was indicated to degrade at an appropriate rate and effectively increase osteoblast cell differentiation both *in vitro* and *in vivo* [39]. To evaluate whether the MBG scaffold was coated with PDA, optical and SEM images were obtained, as shown in Fig. 2d and e, suggesting uniformly coated PDA. After coating, the scaffolds became gray with little shape change, and both scaffolds possessed macro/micro interconnected pore structures, with macropores of 200–500 μm and micropores of 1–2 μm. These images suggest that MBG-PDA scaffolds were successfully fabricated. The morphology of PDA-coated and liposome-loaded MBG scaffolds is shown in Fig. 2f, showing a large amount of TSLs on the scaffold. The nanosized liposomes clumped together due to freeze-drying, but they were indeed localized on the scaffold.

3.2. Photothermal triggered release of payloads in vitro and in vivo

The controllable release platform relies on three critical elements: TSL functioning as a valve of teriparatide, PDA as an effective heater, and NIR light as a photothermal switch. Compared with the MBG scaffolds, the MBG-PDA scaffolds exhibited excellent photothermal effects *in vitro*, as shown in Fig. 3a and b. The temperature on the surface of MBG-PDA scaffolds rose rapidly from room temperature to 42 °C within 40 s and then dropped to 37 °C in 25 s after removing the radiation source. In comparison, the temperature on the surface of the MBG scaffolds did not change within 90 s. Similar results were also observed *in vivo* due to the strong penetration of near-infrared light, as presented in Fig. 3c and d.
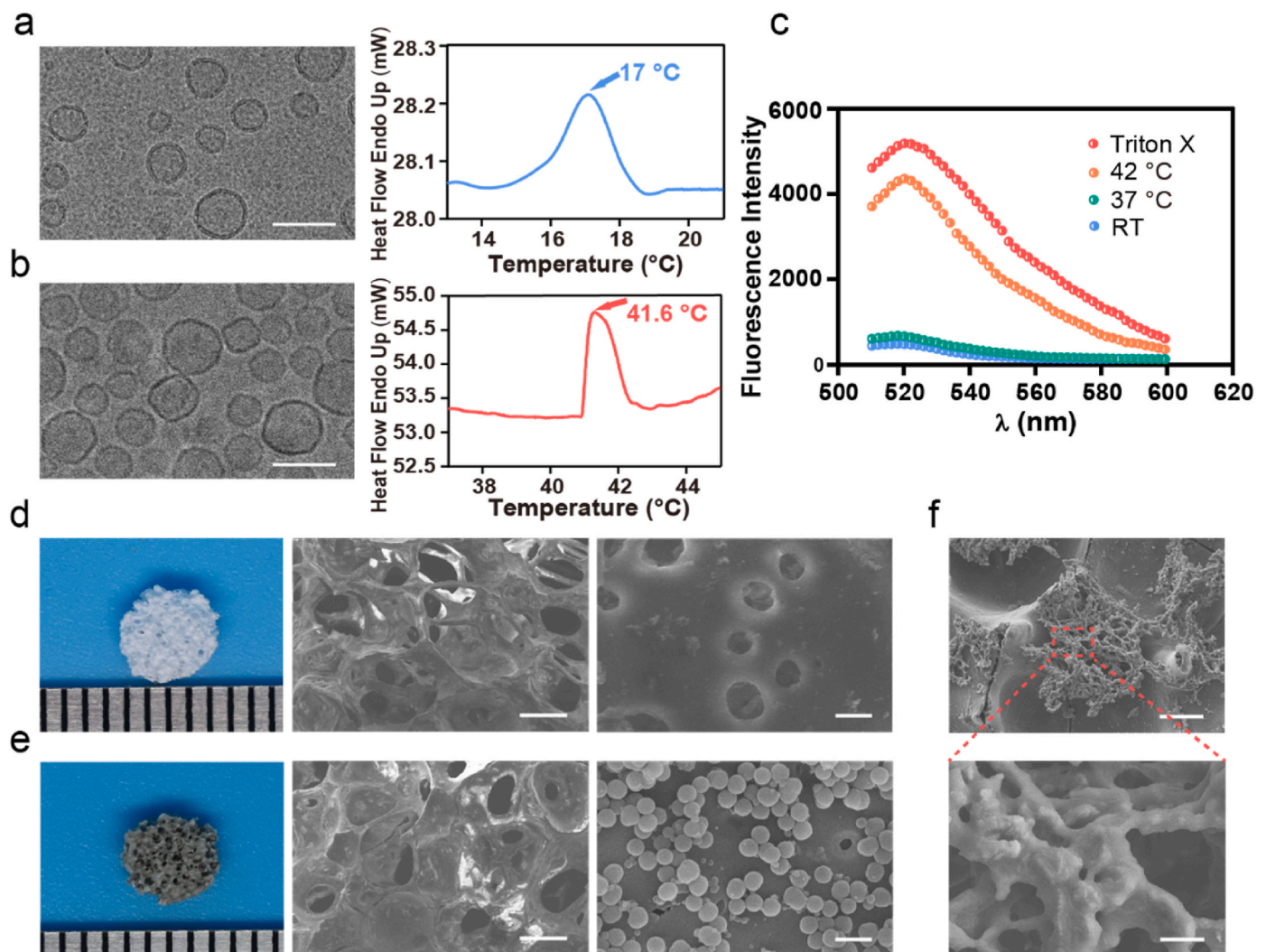
Fig. 2. Characterization of liposomes and scaffolds. a) Cryo-TEM image of DEPC liposomes and DSC spectra showing the T_m at 17 °C; the scale bar is 100 nm. b) Cryo-TEM image of DPPC liposomes and DSC spectra showing the T_m at 41.6 °C; the scale bar is 100 nm. c) Fluorescence intensity of calcein released from DPPC liposomes at room temperature (RT), 37 °C and 42 °C, or in 1% Triton X solution. d, e) Morphology of the MBG scaffolds and PDA-MBG scaffolds at different scales by camera and SEM, respectively; the scale bars are 200 μm (left) and 1 μm (right). f) SEM images of PDA-MBG scaffolds loaded with teriparatide-encapsulated DPPC liposomes after freeze-drying; the scale bars are 500 μm (top) and 3 μm (down).

Interestingly, the temperature rose more quickly *in vivo* than that *in vitro*, up to 42 °C within 30 s, and then decreased to 37 °C in less than 15 s, which was attributed to the higher initial temperature *in vivo*. Irradiation time of 40 s *in vitro* and 30 s *in vivo* were chosen for the subsequent experiments in this article. For pulsatile photothermal responsive release, a reversible phase change of TSL and long-term payload retention should also be considered. Fig. 3e shows that upon irradiation for 40 s, calcein was released immediately on the surface of the platform and could also be detected when the platform was irradiated again after 5 min.

The effective pulsatile release was further traced by *in vivo* fluorescence imaging for a longer time, as shown in Fig. 3f–h and Fig. S1. The released calcein accumulated on the platform after irradiation for 30 s, consistent with the photothermal effect results *in vivo*. Inspiringly, this responsive release behavior lasted for 7 days, although the release amount decreased from the third to the seventh day. This result suggests that liposomes were relatively stable in the cranial bone defect site, and by controlling the irradiation time, the long-term pulsatile and customizable release of teriparatide could be realized on our platforms.

Nontoxic liposomes with different T_m values can be easily synthesized and thereby regulate the release rate of drugs under different

pathological conditions, which have already been commercialized in the clinic [40]. Our results showed that when the ambient temperature reached the T_m of the TSLs, the payloads encapsulated in the liposomes diffused quickly. In contrast, the diffusion was very slow below the T_m, enabling stable retention of payloads and thus pulsatile release behavior. The PDA coating endowed the platform with excellent photothermal effects, with the temperature rising to 42 °C within 30 s at a power density of 0.5 W cm^{-2}. More importantly, the temperature of our platform decreased rapidly within 15 s *in vivo*. This decreasing rate was much faster than that of other NIR-triggered materials [25,41], which contributed to maintaining the released teriparatide bioactivity. The assignments are included (i) Whether or not the encapsulated teriparatide was released and (ii) the release amount could be precisely regulated by the DPPC liposome-loaded platform.

3.3. Pulsatile and continuous release of teriparatide in vitro and cell behavior regulation of platforms

Further evaluation was conducted to confirm the pulsatile teriparatide release on our platform. As the stem cell differentiation was minimally influenced by the PDA coating or NIR irradiation [42], the
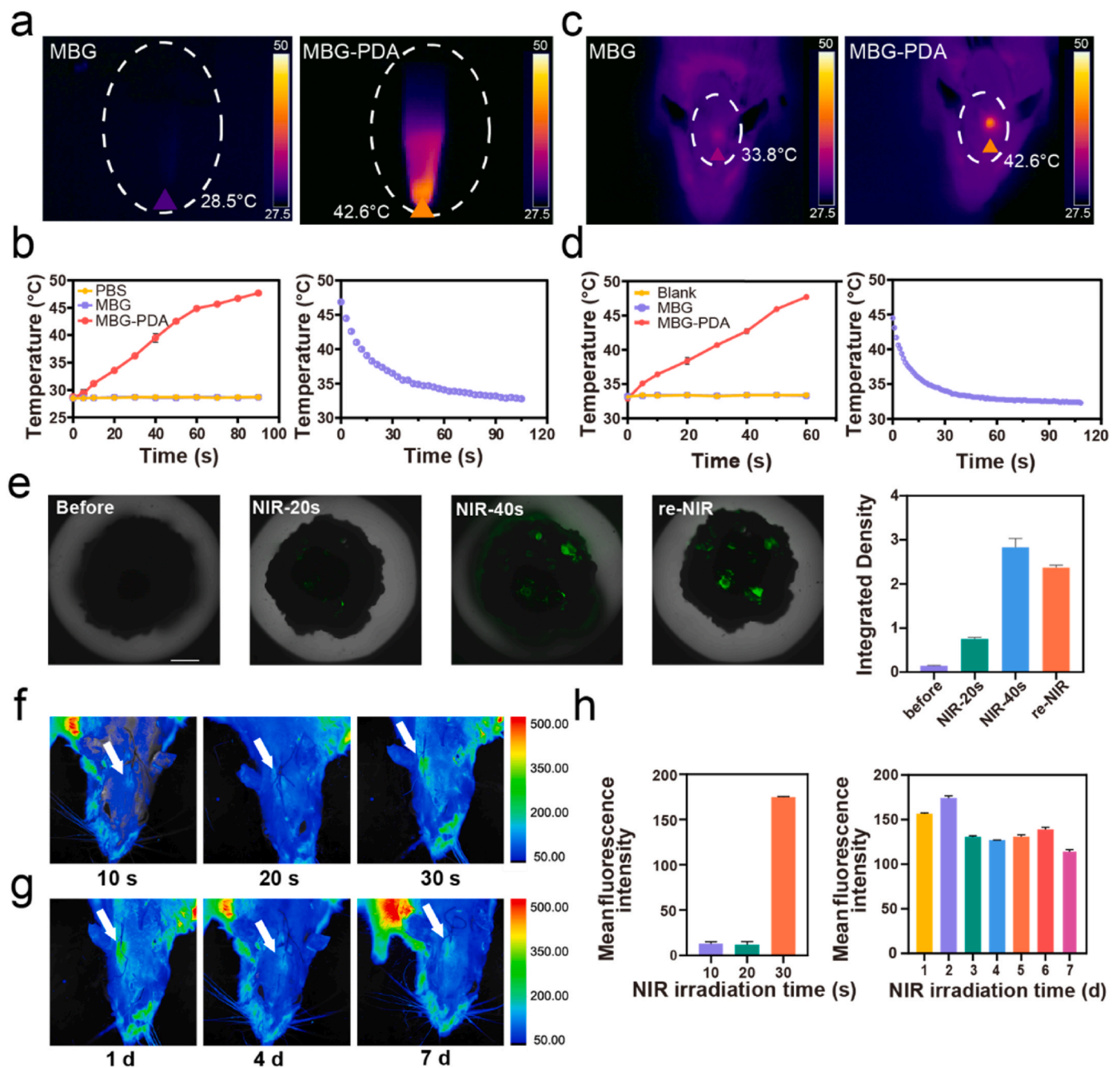
Fig. 3. The photothermal effect of scaffolds and the controllable release of payloads from liposomes or platforms *in vitro* and *in vivo*. a,b) Infrared images of scaffolds with or without coating upon irradiation, and the typical plot of the time-dependent temperature increase as well as their cooling behaviors *in vitro*. c, d) Infrared images of scaffolds with or without coating upon irradiation and the typical plot of the time-dependent temperature increase as well as their cooling behaviors *in vivo*. e) *In vitro* release of calcein from the Pulsatile group scaffold by laser scanning confocal microscopy. The scaffold was irradiated by NIR light for 0 s (NIR-0 s), 20 s (NIR-20 s), and 30 s (NIR-30 s) and then irradiated for 30 s after 5 min (re-NIR); the scale bar is 1 mm. f) Fluorescence images of calcein released from Pulsatile group scaffolds *in vivo,* indicating that the release amount increases as the irradiation time increases. g) Fluorescence images showing the long-term release effect *in vivo*. h) Quantitative analysis of mean fluorescence intensity indicating that the release amount of payloads is controllable and persistent.

Continuous group was established using MBG scaffolds without PDA coating to simplify the experimental variables. As exhibited in Fig. 4a, pulsatile teriparatide release was successfully realized in the Pulsatile group for 14 days, with a controllable release amount of approximately 6% in most cycles. The stable retention of teriparatide was verified by the almost zero release at a single time point without NIR irradiation. In contrast, 34.7% of the total encapsulated teriparatide on the Continuous group platforms was rapidly released, compared with 12.8% on the Pulsatile platforms in the first 48 h, and then was released at a slower rate over the next 11 days. After 14 days, the cumulative release amount

of teriparatide was 79.1% and 73.7% in the Continuous group and Pulsatile group, respectively. Meanwhile, the MBG scaffolds offer porous structures and will show a better interfacial connection with a highly adhesive PDA layer, showing the well storage of the payloads.

Furthermore, the release amount was detected by a parathyroid hormone ELISA kit, which thus suggested that the bioactivity of most teriparatide was maintained due to the antigen-antibody binding principle. The teriparatide from the Continuous group could be released when the temperature of the experiment (37 °C) was above the *Tm* of DEPC TSL. Our on and off cycles of laser irradiation repeated 14 rounds,
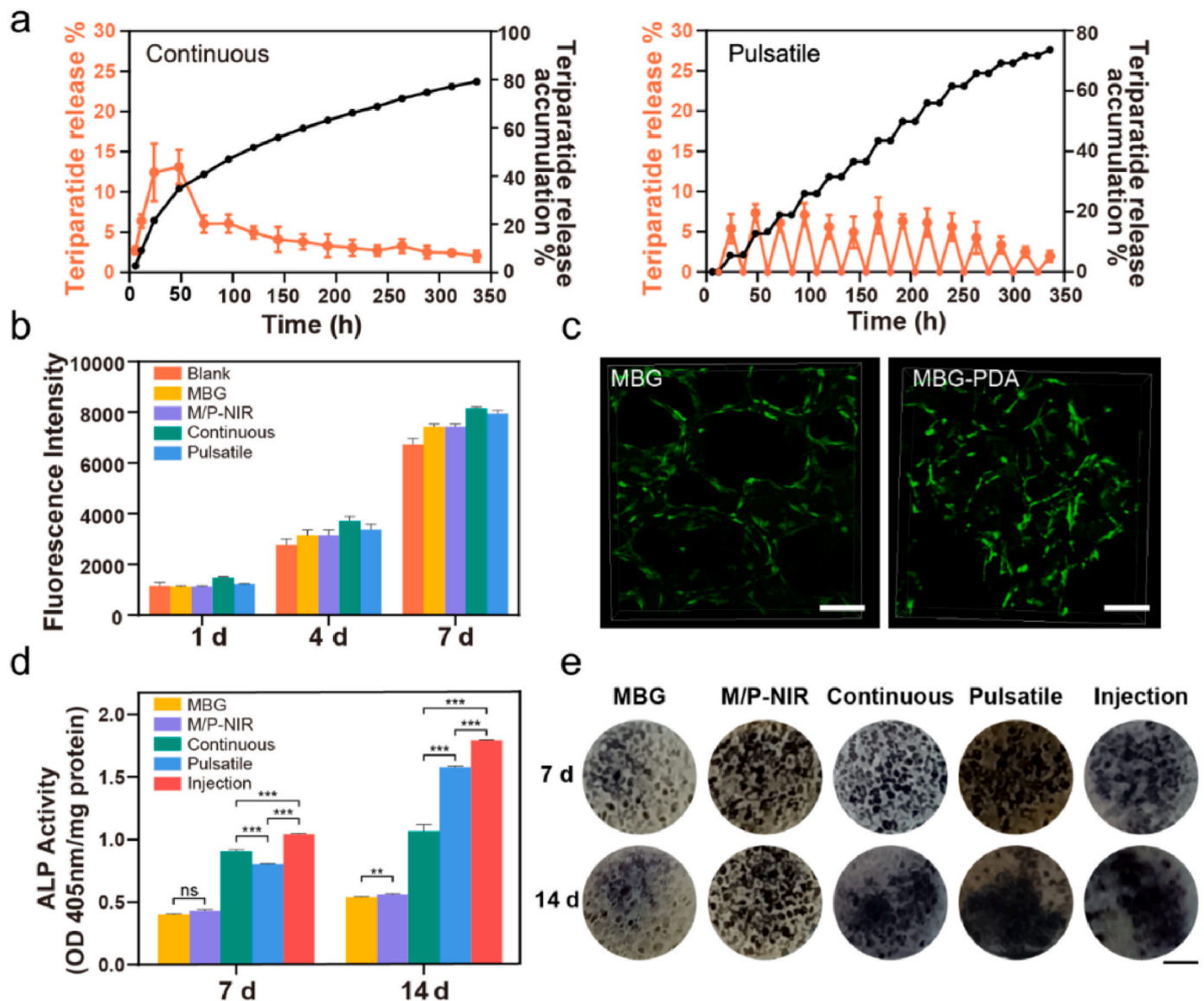
Fig. 4. a) Continuous and pulsatile release profiles of teriparatide occurred on Continuous and Pulsatile group scaffolds *in vitro*, respectively (n = 3). Orange curves represent the amount of single release, while the black curves represent the cumulative release profiles. b) Cell viability of BMSCs on different platforms after 1, 4, and 7 days showing the proliferation ability. c) Cell morphology observation showed that the PDA coating was also suitable for cell spreading; the scale bar is 200 μm. d, e) ALP activity of BMSCs on different platforms after 7 and 14 days; the scale bar is 1 mm **$p < 0.01$, ***$p < 0.001$. (For interpretation of the references to color in this figure legend, the reader is referred to the Web version of this article.)

with good bioactivity of most released teriparatide in each round, which lasted longer than other pulsatile release materials [25,43]. More interestingly, regulating the irradiation time or duration spatiotemporally can also tune the release amount in every cycle or the therapeutic cycle times. The circular dichroism curves of native teriparatide and released teriparatide suggested that a short irradiation time did not damage the bioactivities of this hormone (Fig. S2). The compression strength of the different scaffolds was all over 2 Mpa (Fig. S3), which is within the same range as the normal cancellous bone suggesting that they are sufficient for osteoporotic condition [44].

Cell proliferation and cell adhesion were slightly influenced by PDA coating, TSLs or NIR light, as shown in Fig. 4b and c. By day 4 and day 7, the number of proliferating BMSCs increased by 2-fold vs. day 1 in all groups, with little difference among the blank control, MBG group, and M/P-NIR groups. The number of cells seeded on platforms containing teriparatide increased slightly compared to those without teriparatide. BMSCs spread very well on both the MBG scaffold and MBG-PDA scaffold. The ALP activity of BMSCs indicated that teriparatide improved the

osteogenic differentiation of BMSCs, that the continuous release of teriparatide stimulation was stronger by day 7, and that the pulsatile teriparatide release stimulation was stronger by day 14 (Fig. 4d and e). This improvement may be attributed to the osteoclast differentiation stimulation of teriparatide continuous release in the later stage [45]. Alizarin Red staining (ARS) were also performed for visualization (Fig. S4), and showed a coincident result with ALP staining. Meanwhile, the protein expression of OCN was analyzed using immunofluorescence staining. As shown in Fig. S5, the pulsatile teriparatide release significantly promoted OCN expression compared to Continuous group. All above results confirmed the bioactivity of released teriparatide.

3.4. In vivo evaluation of osteoporotic bone tissue regeneration with a cranial defect model

To verify the osteoporotic condition of the bones prior to defect creation and treatment, micro-CT and histological staining were conducted after the 6-week development of osteoporosis. Both the coronal

and transaxial views of the femur showed the obvious bone loss in the OVX group (Fig. 5a and b). The microarchitectural parameters of the distal femur confirmed the above results (Fig. 5c and Fig. S6). Meanwhile, the number of bone trabeculae decreased (Fig. 5d) further demonstrated the osteoporotic condition in OVX group. To determine the optimal teriparatide release mode to exert the desired anabolic action in osteoporotic bone regeneration, accurate pulsatile and continuous scaffolds were compared in identical experimental setups to assess the outcomes of osteoporotic bone regeneration in a cranial defect model. Tissue morphogenesis and mineralized matrix development at the defect sites were examined using 3D (Fig. 5e and Figs. S7a) and 2D (Fig. 5f and Fig. S7b) analysis by micro-CT. The defect in the Sham group remained a large cavity after 4 weeks, which suggested that the osteoporotic rats could not repair the cranial defects by themselves. In the MBG and M/P-NIR groups, without releasing teriparatide, bone formation was still incomplete. Moreover, the Continuous group exhibited less bone formation than the Injection group, as continuous infusions of teriparatide resulted in a persistent elevation of the serum teriparatide concentration and led to greater bone resorption [46]. In contrast, the Pulsatile group resulted in the best bone regeneration among all groups at both time points. Interestingly, in the MBG, M/P-NIR, Injection and Continuous groups, there was no obvious formation of bone tissue in the center of the defects over time, while there was strong tissue regeneration at the center of the defect sites in the Pulsatile group. This regeneration may be attributed to the fact that local pulsatile teriparatide release and interconnected porous structure of MBG scaffold could prevent or partially reverse bone loss in osteoporotic rats and accelerate the formation of osteoporotic bone tissue inside the scaffold. As we know, in clinic, daily injection of teriparatide is mainly used for the treatment of osteoporosis via inhibiting osteoclast activity and stimulating bone formation [8]. The purpose of our study is to explore the possibility to use teriparatide for local bone regeneration. Our study showed an expected efficiency of systemic anti-osteoporosis, and a limited bone formation at the defect stie for the daily injection of teriparatide group, which was consistent with the previous report [14]. We thought this might be attributed to a low dosage of teriparatide at the bone defect site for daily injection of teriparatide group.

The microarchitectural parameters of the newly formed bone within the cranial defect confirm the above results (Fig. 5g–l). The BV in the Injection group (1.51 ± 0.58 mm^3) was larger than that in the Sham, MBG, M/P-NIR and Continuous groups (0.14 ± 0.05 mm^3, 0.4 ± 0.2 mm^3, 0.48 ± 0.3 mm^3, and 0.66 ± 0.33 mm^3, respectively) at 8 weeks, while the Pulsatile group (2.83 ± 0.61 mm^3) achieved the largest volume of new bone formation (Fig. 5g). Notably, the Tb.Th (Fig. 5h), BS (Fig. 5i), Tb.N (Fig. 5j), and BV/TV (Fig. 5k) showed a similar trend. However, the Tb.Sp (Fig. 5l) was the smallest in the Pulsatile group, suggesting the densest bone regeneration. These results indicate that local precise pulsatile release of teriparatide could greatly prevent bone loss and promote bone healing in osteoporotic bone defects.

Histological staining analysis confirmed that a smart platform with precise pulsatile release of teriparatide could enhance the regeneration of critical bone defects in osteoporotic rats. Fig. 6a and Fig. S8 showed the H&E staining of the specimens at 4 and 8 weeks after implantation. Minimum inflammation was observed in all groups. In the Sham group, the defect area was filled with little loose tissue (with erythrocyte infiltration) at 4 weeks, and a small amount of blue-stained newly formed bone matrix with loose connective tissue appeared in the defect region after 8 weeks. The MBG and Continuous groups showed no obvious bone formation in the osteoporotic bone defect, and only a small amount of loose connective tissue surrounded the scaffolds, while the M/P-NIR group showed notable degradation with abundant loose tissue filling the defect area. The Injection group was filled with little bone matrix, while the largest amount of mature, dense bone tissue appeared in the Pulsatile group. These results reveal that pulsatile release can efficiently stimulate bone regeneration in the osteoporotic microenvironment. MT staining, as a specific staining method for collagen fibers,

can also be used to evaluate the formation and maturation of bone tissue (Fig. 6b and Fig. S9). In the Sham group, loose connective tissue filled the defect sites, and there were no obvious collagen fibers, while in the Injection and M/P-NIR groups, a large amount of immature collagen (blue regions) was observed. The largest area of robust, mature collagen (red regions) appeared in the Pulsatile group after 8 weeks, which showed very impressive osteogenic ability. TRAP staining (Fig. 6c and Fig. S10) showed that the Continuous group had an increased number of osteoclasts compared to the other five controls at 4 weeks, with most of the TRAP-positive cells distributed throughout the fibrous tissue inside the scaffold. In contrast, the number and area of positive osteoclasts in the Pulsatile group were over than those in the other groups at 8 weeks, and a variety of osteoclasts were aligned along the new bone, indicating intense bone remodeling. Meanwhile, with the enhanced activity of osteoclasts, the payloads will be continuously degraded, to leave extra space for the bone regeneration.

To investigate the possible osteogenic-related pathways activated during the bone regeneration process with intelligent drug delivery, IHC staining was performed. The results demonstrated the most intense expression of OPN (Fig. S11) and Runx2 (Fig. S12) in the Pulsatile group. OPN, a secreted acidic protein, is an important osteogenic marker [47]. The expression level of OPN in the Pulsatile group was remarkably higher than that in the other groups at both time points (Fig. S13). Runx2, a molecular hub integration for Wnt and bone morphogenetic protein signals [48], is important in osteoblast differentiation. The expression levels of Runx2 in the Pulsatile group were significantly higher than those in the other groups after 8 weeks (Fig. S14). These results indicate that precise local pulsatile release could upregulate OPN and Runx2 expression and further mediate specific osteogenesis activities, especially in the osteoporotic model, by increasing remodeling in combination with a positive remodeling balance [9].

3.5. In vivo evaluation of the systemic effect of the local precise teriparatide platform

As the femur and lumbar vertebra are the most common sites of osteoporotic fractures in the human body, femur and lumbar vertebra from the different groups were examined using micro-CT to assess the potential systemic anabolic effects of local pulsatile teriparatide releases (Fig. 7). As expected, 8 weeks of injection significantly increased trabecular and cortical bone volumes [2,49]. The Pulsatile group accelerated osteoporotic bone regeneration of the femur and lumbar vertebra more than the other groups except for the Injection group. Teriparatide was continuously released from the local device, however, it did not affect the trabecular and cortical bone. The volume of the trabecular and cortical bone remained unchanged when compared to that of the Sham, MBG, M/P-NIR groups (Fig. 7a–d). The parameters of the femur confirm the above results (Fig. 7e–j and Fig. S115). The BV/TV in the Pulsatile group ($28.33 \pm 4.84\%$ for 8 weeks) was larger than that of the Sham, M/P-NIR MBG, and Continuous groups, while the Injection group ($41.02 \pm 2.96\%$) achieved the largest volume of new bone regeneration (Fig. 7e). Tb.Th (Fig. 7f), Tb.N (Fig. 7g), BV (Fig. 7j), and BS (Fig. S15) showed similar trends, while the Tb.Sp (Fig. 7h) and the SMI (Fig. 7i) were the smallest in the Injection group, suggesting a higher quality of bone tissue regeneration. Thus, to a certain extent, the local pulsatile release of teriparatide has a therapeutic effect on osteoporosis of the whole body.

Compared with current biomaterials for the repair of osteoporotic bone defects, this TSL/PDA/MBG platform shows strong osteogenic ability in terms of cranial BV/TV, femoral BV/TV, and experimental period (Fig. S16). To the best of our knowledge, the variety of biomaterials for treating osteoporotic bone defects is usually focused on only the skull [50–53] or femur [12,54–60] [61-67]. Even when both the skull and femur were evaluated, they were rarely reported for a cranial BV/TV beyond 27.16% while maintaining a femoral BV/TV of 28.33% as well as a relatively short experimental period [68]. Optimized
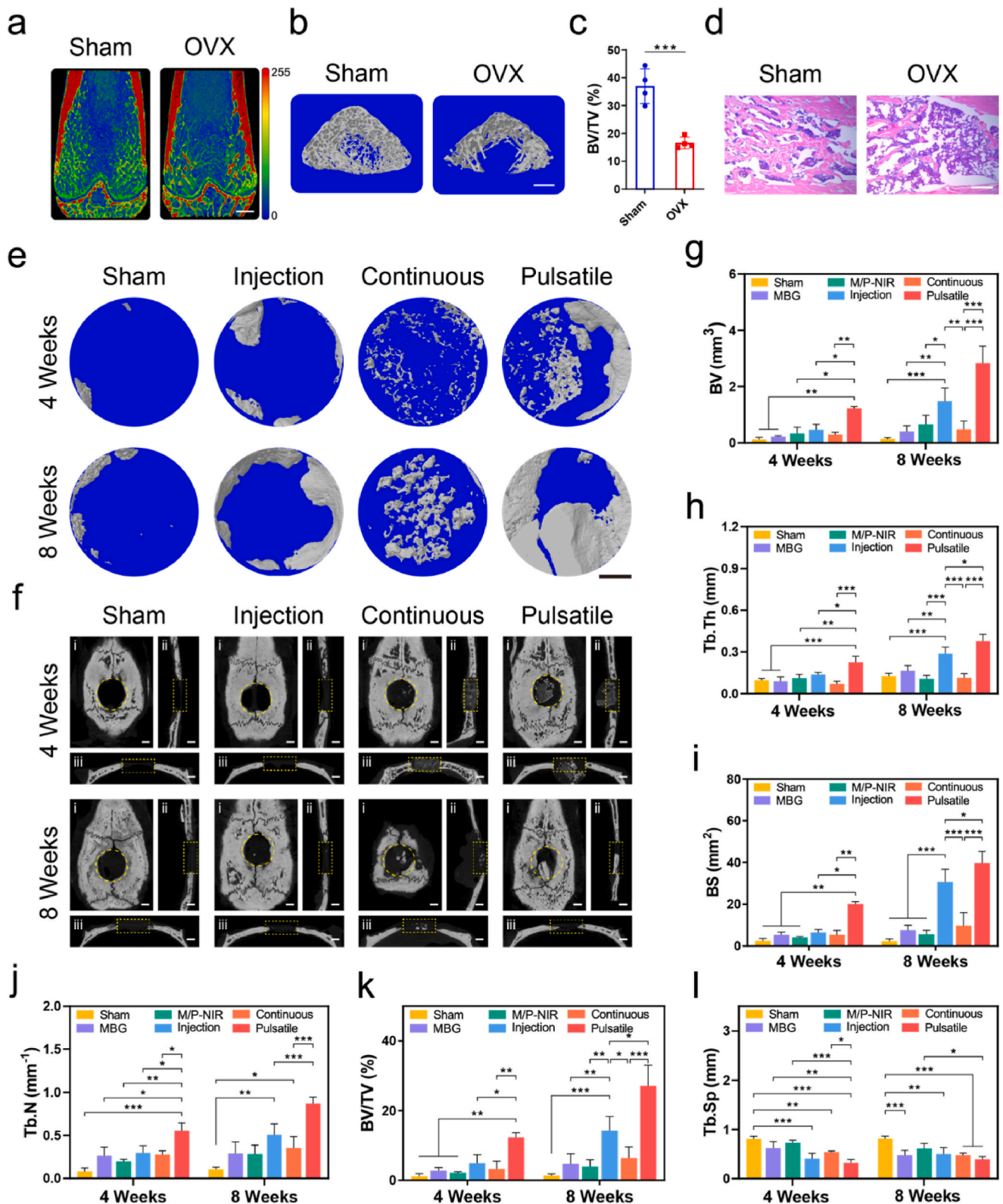
Fig. 5. a) Coronal-view micro-CT 3D reconstructed images of the femur in Sham and OVX rats; the scale bar is 500 μm; b) Micro-CT 3D reconstructed images of transaxial view of the femur in Sham and OVX rats; the scale bar is 1 mm; c) Morphological parameters BV/TV quantified by CTAn software; d) Representative images of H&E staining of the femur in Sham and OVX rats; the scale bar is 400 μm; e) Micro-CT 3D reconstructed images of the defect site after 4 weeks and 8 weeks of regeneration; the scale bar is 1 mm. f) Micro-CT 2D images of coronary (i), sagittal (ii), and transaxial (iii) sections of the defect area with surrounding tissue after 4 weeks and 8 weeks of regeneration; the scale bar is 1 mm. g) Morphological parameters BV quantified by CTAn software. h) Morphological parameters Tb.Th quantified by CTAn software. i) Morphological parameters BS quantified by CTAn software. j) Morphological parameters Tb.N quantified by CTAn software. k) Morphological parameters BV/TV quantified by CTAn software. l) Morphological parameters Tb.Sp quantified by CTAn software. $*p < 0.05$, $**p < 0.01$, $***p < 0.001$.
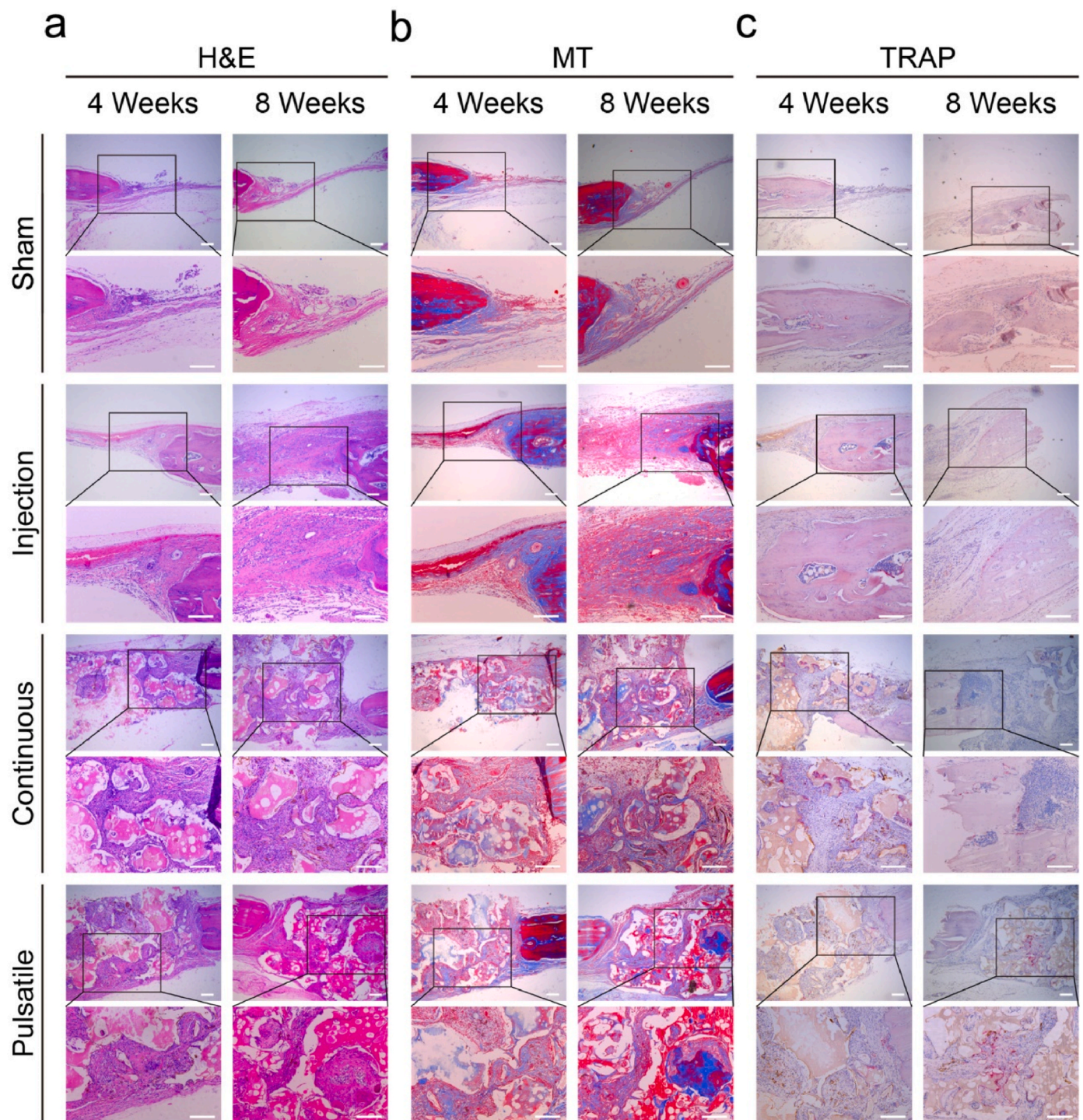
Fig. 6. a) Optical photographs and their magnified images for H&E staining in different platforms for 4 and 8 weeks. b) Optical photographs and their magnified images for MT staining in different platforms for 4 and 8 weeks. c) Optical photographs and their magnified images for TRAP staining in different platforms for 4 and 8 weeks. The scale bar is 200 μm.

biomaterials are designed to achieve the best regeneration in the least time; thus, an inverted Z-axis is defined to highlight the rapid repair ability. Therefore, this bioactive platform with precise pulsatile release of teriparatide takes a step forward optimizing local and systemic osteoporosis treatment. A detailed comparison is shown in Table S1.

Our platform algorithms that combine rapid local fracture healing and systemic improvement of osteoporosis may be promising in clinical practice to target high-risk individuals with osteoporotic fractures for treatment. Collectively, compared with the previous study [69], there

are three key innovations in this study as below: (1) Excellent stimuli-responsive precise regulation and longer duration. This study realized more accurate regulation by manipulating temperatures (with a heating time within 40 s and a cooling time within 25 s), which endowed a more precise regulation of teriparatide release. More importantly, such an excellent sensitivity extended the release time of teriparatide to 14 days compared with 7 days in the previous study. (2) clinical potential. The key MBG scaffold with interconnected porous structures was degradable and more suitable for tissue growth. FDA-approved TSLs and
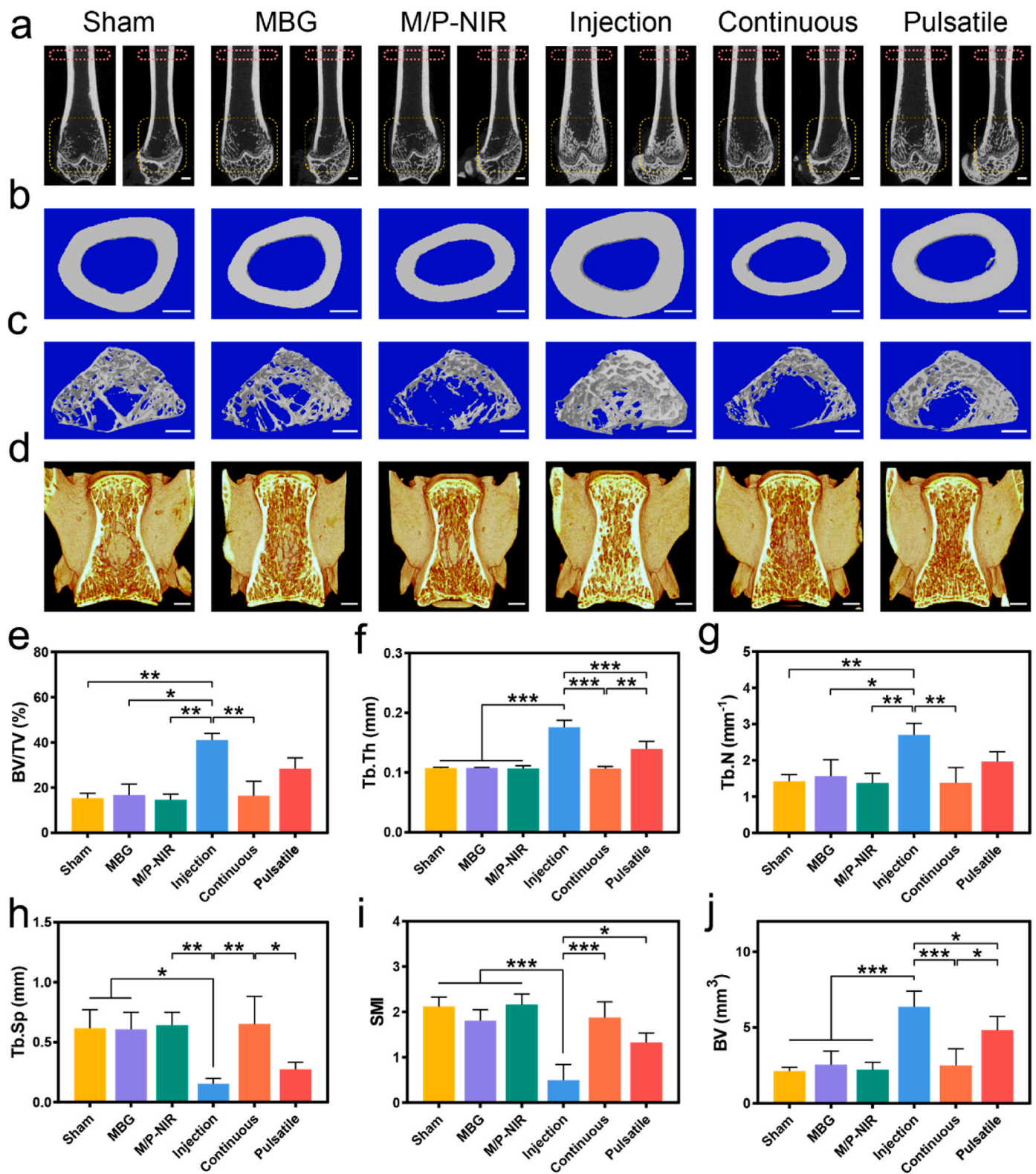
Fig. 7. a) Micro-CT 2D images of coronary and sagittal sections of the femur at 8 weeks; the scale bar is 1 mm. b) Micro-CT 3D reconstructed images of the femoral cortical bone at 8 weeks; the scale bar is 1 mm. c) Micro-CT 3D reconstructed images of the femoral cancellous bone at 8 weeks; the scale bar is 1 mm. d) Micro-CT 3D reconstructed images of the lumbar vertebra at 8 weeks; the scale bar is 1 mm. e) Morphological parameters BV/TV quantified by CTAn software. f) Morphological parameters Tb.Th quantified by CTAn software. g) Morphological parameters Tb.N quantified by CTAn software. h) Morphological parameters Tb.Sp quantified by CTAn software. i) Morphological parameters SMI quantified by CTAn software. j) Morphological parameters BV quantified by CTAn software. $*p < 0.05$, $**p < 0.01$, $***p < 0.001$.

MBG are anticipated in clinical commercialization and translation. (3) Green chemistry. Different from the previous studies, all materials/chemical in our study were easily fabricated without any safety issues. Overall, the evaluation of cryo-electron microscopy indicates the potential stable drug storage system of TSLs. An excellent photothermal effect verifies the higher sensitivity and long-term controllable pulsatile release, presenting strong promotion of osteogenic differentiation of BMSCs *in vitro* and osteoporotic bone regeneration *in vivo*. A net anabolic effect of bone metabolism in the whole body was also observed, indicating the bifunctional of the platform.

4. Conclusion

As a proof-of-concept demonstration, a three-in-one smart platform with TSLs used as a valve, PDA coating used as a heater, and NIR light as a trigger is fabricated to both rejuvenate osteoporotic bone defects and systemically treat osteoporosis. It is an elaborate device to deliver teriparatide to osteoporotic bone defects sensitively and efficiently, preserve teriparatide bioactivity, maintain long-term storage, and induce optimal osteoporotic bone regeneration. Recent progress in the design of sound energy demonstrates excellent dynamic contrast-enhanced and enhanced sensitivity, facilitating excellent quantification *in vivo* regardless of penetration depth. In the future, it would be interesting to combine further novel drug delivery and sound energy, which will overcome the traditional penetration depth and expand the application of this drug delivery system for a variety of diseases.

CRediT authorship contribution statement

Lingbin Che: Conceptualization, Investigation, Data curation, Writing – original draft. **Ying Wang:** Methodology, Investigation, Writing – original draft. **Dongyong Sha:** Software. **Guangyi Li:** Investigation. **Ziheng Wei:** Resources. **Changsheng Liu:** Conceptualization, Resources. **Yuan Yuan:** Supervision, Resources, Funding acquisition, Writing – review & editing. **Dianwen Song:** Conceptualization, Supervision, Project administration, Funding acquisition.

Declaration of competing interest

The authors declare that they have no known competing financial interests or personal relationships that could have appeared to influence the work reported in this paper.

Acknowledgements

Appendix A. Supplementary data

Supplementary data to this article can be found online at https://doi.org/10.1016/j.bioactmat.2022.03.023.

References

[1] D.M. Black, E.J. Geiger, R. Eastell, E. Vittinghoff, B.H. Li, D.S. Ryan, R.M. Dell, A. L. Adams, Atypical femur fracture risk versus fragility fracture prevention with bisphosphonates, N. Engl. J. Med. 383 (8) (2020) 743–753.

[2] E. Canalis, A. Giustina, J.P. Bilezikian, Mechanisms of anabolic therapies for osteoporosis, N. Engl. J. Med. 357 (9) (2007) 905–916.

[3] J.E. Compston, M.R. McClung, W.D. Leslie, Osteoporosis, Lancet 393 (10169) (2019) 364–376.

[4] O. Johnell, J.A. Kanis, An estimate of the worldwide prevalence and disability associated with osteoporotic fractures, Osteoporos. Int. 17 (12) (2006) 1726–1733.

[5] L. Si, T.M. Winzenberg, Q. Jiang, M. Chen, A.J. Palmer, Projection of osteoporosis-related fractures and costs in China: 2010-2050, Osteoporos. Int. 26 (7) (2015) 1929–1937.

[6] B. Yuan, L.N. Wang, R. Zhao, X. Yang, X. Yang, X.D. Zhu, L.M. Liu, K. Zhang, Y. M. Song, X.D. Zhang, A biomimetically hierarchical polyetherketoneketone scaffold for osteoporotic bone repair, Sci. Adv. 6 (50) (2020).

[7] T.A. van Geel, S. van Helden, P.P. Geusens, B. Winkens, G.J. Dinant, Clinical subsequent fractures cluster in time after first fractures, Ann. Rheum. Dis. 68 (1) (2009) 99–102.

[8] R.M. Neer, C.D. Arnaud, J.R. Zanchetta, R. Prince, G.A. Gaich, J.Y. Reginster, A. B. Hodsman, E.F. Eriksen, S. Ish-Shalom, H.K. Genant, O. Wang, B.H. Mitlak, Effect of parathyroid hormone (1-34) on fractures and bone mineral density in postmenopausal women with osteoporosis, N. Engl. J. Med. 344 (19) (2001) 1434–1441.

[9] S. Khosla, L.C. Hofbauer, Osteoporosis treatment: recent developments and ongoing challenges, Lancet Diabetes Endocrinol 5 (11) (2017) 898–907.

[10] D.L. Kendler, F. Marin, C.A.F. Zerbini, L.A. Russo, S.L. Greenspan, V. Zikan, A. Bagur, J. Malouf-Sierra, P. Lakatos, A. Fahrleitner-Pammer, E. Lespessailles, S. Minisola, J.J. Body, P. Geusens, R. Moricke, P. Lopez-Romero, Effects of teriparatide and risedronate on new fractures in post-menopausal women with severe osteoporosis (VERO): a multicentre, double-blind, double-dummy, randomised controlled trial, Lancet 391 (10117) (2018) 230–240.

[11] P.D. Miller, G. Hattersley, B.J. Riis, G.C. Williams, E. Lau, L.A. Russo, P. Alexandersen, C.A. Zerbini, M.Y. Hu, A.G. Harris, L.A. Fitzpatrick, F. Cosman, C. Christiansen, A.S. Investigators, Effect of abaloparatide vs placebo on new vertebral fractures in postmenopausal women with osteoporosis: a randomized clinical trial, JAMA 316 (7) (2016) 722–733.

[12] B. Yuan, L. Wang, R. Zhao, X. Yang, X. Yang, X. Zhu, L. Liu, K. Zhang, Y. Song, X. Zhang, A biomimetically hierarchical polyetherketoneketone scaffold for osteoporotic bone repair, Sci. Adv. 6 (50) (2020).

[13] Y. Zeng, M. Zhou, L. Chen, H. Fang, S. Liu, C. Zhou, J. Sun, Z. Wang, Alendronate loaded graphene oxide functionalized collagen sponge for the dual effects of osteogenesis and anti-osteoclastogenesis in osteoporotic rats, Bioact Mater 5 (4) (2020) 859–870.

[14] M. Dang, A.J. Koh, X.B. Jin, L.K. McCauley, P.X. Ma, Local pulsatile PTH delivery regenerates bone defects via enhanced bone remodeling in a cell-free scaffold, Biomaterials 114 (2017) 1–9.

[15] N. Amani, H.A. Javar, F.A. Dorkoosh, M.R. Rouini, M. Amini, M. Sharifzadeh, S. Boumi, Preparation and pulsatile release evaluation of teriparatide-loaded multilayer implant composed of polyanhydride-hydrogel layers using spin coating for the treatment of osteoporosis, J. Pharm. Innov. 22.

[16] P. Davoodi, L.Y. Lee, Q. Xu, V. Sunil, Y. Sun, S. Soh, C.-H. Wang, Drug delivery systems for programmed and on-demand release, Adv. Drug Deliv. Rev. 132 (2018) 104–138.

[17] P. Davoodi, W.C. Ng, W.C. Yan, M.P. Srinivasan, C.-H. Wang, Double-Walled microparticles-embedded self-cross-linked, injectable, and antibacterial hydrogel for controlled and sustained release of chemotherapeutic agents, ACS Appl. Mater. Interfaces 8 (35) (2016) 22785–22800.

[18] P. Davoodi, F. Feng, Q. Xu, W.-C. Yan, Y.W. Tong, M.P. Srinivasan, V.K. Sharma, C.-H. Wang, Coaxial electrohydrodynamic atomization: microparticles for drug delivery applications, J. Contr. Release 205 (2015) 70–82.

[19] P. Davoodi, W.C. Ng, M.P. Srinivasan, C.-H. Wang, Codelivery of anti-cancer agents via double-walled polymeric microparticles/injectable hydrogel: a promising approach for treatment of triple negative breast cancer, Biotechnol. Bioeng. 114 (12) (2017) 2931–2946.

[20] T.M. Allen, P.R. Cullis, Liposomal drug delivery systems: from concept to clinical applications, Adv. Drug Deliv. Rev. 65 (1) (2013) 36–48.

[21] J.C. Kraft, J.P. Freeling, Z. Wang, R.J.Y. Ho, Emerging Research and clinical development trends of liposome and lipid nanoparticle drug delivery systems, J. Pharmaceut. Sci. 103 (1) (2014) 29–52.

[22] G. Kong, R.D. Braun, M.W. Dewhirst, Characterization of the effect of hyperthermia on nanoparticle extravasation from tumor vasculature, Cancer Res. 61 (7) (2001) 3027–3032.

[23] Y.C. Wang, M.S. Shim, N.S. Levinson, H.W. Sung, Y.N. Xia, Stimuli-responsive materials for controlled release of theranostic agents, Adv. Funct. Mater. 24 (27) (2014) 4206–4220.

[24] Y. Lu, A.A. Aimetti, R. Langer, Z. Gu, Bioresponsive materials, Nat. Rev. Mater. 2 (1) (2017) 17.

[25] J.J. Xue, C.L. Zhu, J.H. Li, H.X. Li, Y.N. Xia, Integration of phase-change materials with electrospun fibers for promoting neurite outgrowth under controlled release, Adv. Funct. Mater. 28 (15) (2018).

[26] J.J. Xue, T. Wu, J.C. Qiu, Y.N. Xia, Spatiotemporally controlling the release of biological effectors enhances their effects on cell migration and neurite outgrowth, Small Methods 13.

[27] A. Donsante, J.J. Xue, K.M. Poth, N.S. Hardcastle, B. Diniz, D.M. O'Connor, Y. N. Xia, N.M. Boulis, Controlling the release of neurotrophin-3 and chondroitinase ABC enhances the efficacy of nerve guidance conduits, Adv. Healthc. Mater. 9 (14) (2020) 10.

[28] J.C. Qiu, D. Huo, Y.N. Xia, Phase-change materials for controlled release and related applications, Adv. Mater. 32 (25) (2020) 21.

[29] P. Yang, F. Zhu, Z. Zhang, Y. Cheng, Z. Wang, Y. Li, Stimuli-responsive Polydopamine-Based Smart Materials, Chem Soc Rev, 2021.

[30] I.H. Kim, T. Yun, J.E. Kim, H. Yu, S.P. Sasikala, K.E. Lee, S.H. Koo, H. Hwang, H. J. Jung, J.Y. Park, H.S. Jeong, S.O. Kim, Mussel-inspired defect engineering of graphene liquid crystalline fibers for synergistic enhancement of mechanical strength and electrical conductivity, Adv. Mater. (2018), e1803267.

[31] C. Schlaich, M.J. Li, C. Cheng, I.S. Donskyi, L.X. Yu, G. Song, E. Osorio, Q. Wei, R. Haag, Mussel-inspired polymer-based universal spray coating for surface modification: fast fabrication of antibacterial and superhydrophobic surface coatings, Adv. Mater. Interfac. 5 (5) (2018) 8.

[32] G. Thrivikraman, A. Athirasala, R. Gordon, L. Zhang, R. Bergan, D.R. Keene, J. M. Jones, H. Xie, Z. Chen, J. Tao, B. Wingender, L. Gower, J.L. Ferracane, L. E. Bertassoni, Rapid fabrication of vascularized and innervated cell-laden bone models with biomimetic intrafibrillar collagen mineralization, Nat. Commun. 10 (1) (2019) 3520.

[33] P.C. Qiu, M.B. Li, K. Chen, B. Fang, P.F. Chen, Z.B. Tang, X.F. Lin, S.W. Fan, Periosteal matrix-derived hydrogel promotes bone repair through an early immune regulation coupled with enhanced angio- and osteogenesis, Biomaterials 227 (2020).

[34] L.T. Jiang, W.J. Zhang, L. Wei, Q. Zhou, G.Z. Yang, N.D. Qian, Y. Tang, Y.M. Gao, X.Q. Jiang, Early effects of parathyroid hormone on vascularized bone regeneration and implant osseointegration in aged rats, Biomaterials 179 (2018) 15–28.

[35] K. Ogata, M. Osugi, T. Kawai, Y. Wakayama, K. Sakaguchi, S. Nakamura, W. Katagiri, Secretomes of mesenchymal stem cells induce early bone regeneration by accelerating migration of stem cells, J. Oral Max Surg. Med. 30 (5) (2018) 445–451.

[36] A. Ho-Shui-Ling, J. Bolander, L.E. Rustom, A.W. Johnson, F.P. Luyten, C. Picart, Bone regeneration strategies: engineered scaffolds, bioactive molecules and stem cells current stage and future perspectives, Biomaterials 180 (2018) 143–162.

[37] Y. Liu, Z. Yang, L. Wang, L. Sun, B.Y.S. Kim, W. Jiang, Y. Yuan, C. Liu, Spatiotemporal immunomodulation using biomimetic scaffold promotes endochondral ossification-mediated bone healing, Adv. Sci. 8 (11) (2021), e2100143.

[38] A. Agarwal, M.A. Mackey, M.A. El-Sayed, R.V. Bellamkonda, Remote triggered release of doxorubicin in tumors by synergistic application of thermosensitive liposomes and gold nanorods, ACS Nano 5 (6) (2011) 4919–4926.

[39] W. Tang, D. Lin, Y. Yu, H. Niu, H. Guo, Y. Yuan, C. Liu, Bioinspired trimodal macro/micro/nano-porous scaffolds loading rhBMP-2 for complete regeneration of critical size bone defect, Acta Biomater 32 (2016) 309–323.

[40] L.H. Lindner, M. Hossann, M. Vogeser, N. Teichert, K. Wachholz, H. Eibl, W. Hiddemann, R.D. Issels, Dual role of hexadecylphosphocholine (miltefosine) in thermosensitive liposomes: active ingredient and mediator of drug release, J. Contr. Release 125 (2) (2008) 112–120.

[41] D. Zhu, M. Lyu, Q. Huang, M. Suo, Y. Liu, W. Jiang, Y. Duo, K. Fan, Stellate plasmonic exosomes for penetrative targeting tumor NIR-II thermo-radiotherapy, ACS Appl. Mater. Interfaces 12 (33) (2020) 36928–36937.

[42] J. Li, C.W.T. Leung, D.S.H. Wong, J. Xu, R. Li, Y. Zhao, C.Y.Y. Yung, E. Zhao, B. Z. Tang, L. Bian, Photocontrolled SiRNA delivery and biomarker-triggered luminogens of aggregation-induced emission by up-conversion NaYF4:Yb(3+)Tm (3+)@SiO2 nanoparticles for inducing and monitoring stem-cell differentiation, ACS Appl. Mater. Interfaces 11 (25) (2019) 22074–22084.

[43] P. Yuan, T. Yang, T. Liu, X. Yu, Y. Bai, Y. Zhang, X. Chen, Nanocomposite hydrogel with NIR/magnet/enzyme multiple responsiveness to accurately manipulate local drugs for on-demand tumor therapy, Biomaterials 262 (2020) 120357.

[44] O. Chaudhuri, J. Cooper-White, P.A. Janmey, D.J. Mooney, V.B. Shenoy, Effects of extracellular matrix viscoelasticity on cellular behaviour, Nature 584 (7822) (2020) 535–546.

[45] N. Fratzl-Zelman, K. Wesseling-Perry, R.E. Makitie, S. Blouin, M.A. Hartmann, J. Zwerina, V.V. Valimaki, C.M. Laine, M.J. Valimaki, R.C. Pereira, O. Makitie, Bone material properties and response to teriparatide in osteoporosis due to WNT1 and PLS3 mutations, Bone 146 (2021) 115900.

[46] C.S. Tam, J.N. Heersche, T.M. Murray, J.A. Parsons, Parathyroid hormone stimulates the bone apposition rate independently of its resorptive action: differential effects of intermittent and continuous administration, Endocrinology 110 (2) (1982) 506–512.

[47] L. Che, Z. Lei, P. Wu, D. Song, A 3D printable and bioactive hydrogel scaffold to treat traumatic brain injury, Adv. Funct. Mater. 29 (39) (2019) 1904450.

[48] F. Long, Building strong bones: molecular regulation of the osteoblast lineage, Nat. Rev. Mol. Cell Biol. 13 (1) (2011) 27–38.

[49] A.J. Koh, C.M. Novince, X. Li, T. Wang, R.S. Taichman, L.K. McCauley, An irradiation-altered bone marrow microenvironment impacts anabolic actions of PTH, Endocrinology 152 (12) (2011) 4525–4536.

[50] K.L. Lin, L.G. Xia, H.Y. Li, X.Q. Jiang, H.B. Pan, Y.J. Xu, W.W. Lu, Z.Y. Zhang, J. Chang, Enhanced osteoporotic bone regeneration by strontium-substituted calcium silicate bioactive ceramics, Biomaterials 34 (38) (2013) 10028–10042.

[51] J.K. Zeng, J.S. Guo, Z.Y. Sun, F.Y. Deng, C.Q. Ning, Y.Z. Xie, Osteoblastic and anti-osteoclastic activities of strontium-substituted silicocarnotite ceramics: in vitro and in vivo studies, Bioactive Materials 5 (3) (2020) 435–446.

[52] X. Wang, D. Zeng, W. Weng, Q. Huang, X. Zhang, J. Wen, J. Wu, X. Jiang, Alendronate delivery on amino modified mesoporous bioactive glass scaffolds to enhance bone regeneration in osteoporosis rats, Artif. Cells Nanomed Biotechnol 46 (sup2) (2018) 171–181.

[53] Y.Y. Zeng, M.R. Zhou, L.F. Chen, H.M. Fang, S.K. Liu, C.C. Zhou, J.M. Sun, Z. X. Wang, Alendronate loaded graphene oxide functionalized collagen sponge for the dual effects of osteogenesis and anti-osteoclastogenesis in osteoporotic rats, Bioactive Materials 5 (4) (2020) 859–870.

[54] E.P. Ghamor-Amegavi, X. Yang, J. Qiu, L. Xie, Z. Pan, J. Wang, X. Zhang, X. Ke, T. Zhao, L. Zhang, Z. Gou, Composition control in biphasic silicate microspheres on stimulating new bone regeneration and repair of osteoporotic femoral bone defect, J. Biomed. Mater. Res. B Appl. Biomater. 108 (2) (2020) 377–390.

[55] B. Yuan, M.G. Raucci, Y. Fan, X. Zhu, X. Yang, X. Zhang, M. Santin, L. Ambrosio, Injectable strontium-doped hydroxyapatite integrated with phosphoserine-tethered poly(epsilon-lysine) dendrons for osteoporotic bone defect repair, J. Mater. Chem. B 6 (47) (2018) 7974–7984.

[56] P. Jia, H. Chen, H. Kang, J. Qi, P. Zhao, M. Jiang, L. Guo, Q. Zhou, N.D. Qian, H. B. Zhou, Y.J. Xu, Y. Fan, L.F. Deng, Deferoxamine released from poly(lactic-co-glycolic acid) promotes healing of osteoporotic bone defect via enhanced angiogenesis and osteogenesis, J. Biomed. Mater. Res. 104 (10) (2016) 2515–2527.

[57] L. Cao, G.W. Liu, Y.K. Gan, Q.M. Fan, F. Yang, X.L. Zhang, T.T. Tang, K.R. Dai, The use of autologous enriched bone marrow MSCs to enhance osteoporotic bone defect repair in long-term estrogen deficient goats, Biomaterials 33 (20) (2012) 5076–5084.

[58] L.M. Li, M.L. Yu, Y. Li, Q. Li, H.C. Yang, M. Zheng, Y. Han, D. Lu, S. Lu, L. Gui, Synergistic anti-inflammatory and osteogenic n-HA/resveratrol/chitosan composite microspheres for osteoporotic bone regeneration, Bioactive Materials 6 (5) (2021) 1255–1266.

[59] H.Y. Quan, Y.W. He, J.J. Sun, W.H. Yang, W. Luo, C. Dou, F. Kang, C.R. Zhao, J. He, X.C. Yang, S.W. Dong, H. Jiang, Chemical self-assembly of multifunctional hydroxyapatite with a coral-like nanostructure for osteoporotic bone reconstruction, ACS Appl. Mater. Interfaces 10 (30) (2018) 25547–25560.

[60] X.Y. Chen, X.L. Sun, X.Y. Yang, L. Zhang, M. Lin, G.J. Yang, C.Y. Gao, Y.B. Feng, J. Yu, Z.R. Gou, Biomimetic preparation of trace element-codoped calcium phosphate for promoting osteoporotic bone defect repair, J. Mater. Chem. B 1 (9) (2013) 1316–1325.

[61] T.L. Li, Z.S. Tao, X.J. Wu, M. Yang, H.G. Xu, Selenium-modified calcium phosphate cement can accelerate bone regeneration of osteoporotic bone defect, J. Bone Miner. Metabol. (2021).

[62] S. Sun, L. Tang, T. Zhao, Y. Kang, L. Sun, C. Liu, Y. Li, F. Xu, Y.X. Qin, D. Ta, Longitudinal effects of low-intensity pulsed ultrasound on osteoporosis and osteoporotic bone defect in ovariectomized rats, Ultrasonics 113 (2021) 106360.

[63] J. Chen, W. Liu, J. Zhao, C. Sun, J. Chen, K. Hu, L. Zhang, Y. Ding, Gelatin microspheres containing calcitonin gene-related peptide or substance P repair bone defects in osteoporotic rabbits, Biotechnol. Lett. 39 (3) (2017) 465–472.

[64] Z.S. Tao, W.S. Zhou, R.T. Zhang, Y. Li, H.G. Xu, S. Wei, Z.Y. Wang, M. Yang, Co-modification of calcium phosphate cement to achieve rapid bone regeneration in osteoporotic femoral condyle defect with lithium and aspirin, Am. J. Transl. Res. 13 (3) (2021) 952–966.

[65] J. Li, C. Deng, W. Liang, F. Kang, Y. Bai, B. Ma, C. Wu, S. Dong, Mn-containing bioceramics inhibit osteoclastogenesis and promote osteoporotic bone regeneration via scavenging ROS, Bioact Mater 6 (11) (2021) 3839–3850.

[66] R. Zhang, M. Yang, Y. Li, H. Liu, M. Ren, Z.S. Tao, Effect of alendronate on the femoral metaphyseal defect under carbamazepine in ovariectomized rats, J. Orthop. Surg. Res. 16 (1) (2021) 14.

[67] W. Liu, J. Huang, F. Chen, D. Xie, L. Wang, C. Ye, Q. Zhu, X. Li, X. Li, L. Yang, MSC-derived small extracellular vesicles overexpressing miR-20a promoted the osteointegration of porous titanium alloy by enhancing osteogenesis via targeting BAMBI, Stem Cell Res. Ther. 12 (1) (2021) 348.

[68] Y. Zeng, M. Zhou, S. Mou, J. Yang, Q. Yuan, L. Guo, A. Zhong, J. Wang, J. Sun, Z. Wang, Sustained delivery of alendronate by engineered collagen scaffold for the repair of osteoporotic bone defects and resistance to bone loss, J. Biomed. Mater. Res. 108 (12) (2020) 2460–2472.

[69] L.J. Kuang, J.H. Huang, Y.T. Liu, X.L. Li, Y. Yuan, C.S. Liu, Injectable hydrogel with NIR light-responsive, dual-mode PTH release for osteoregeneration in osteoporosis, Adv. Funct. Mater. 31 (47) (2021).